

Field-Programmable Topological Torons in Chiral Nematic Liquid Crystals

Adithya Pradeep^{a,*}, Urban Mur^{a,b}, Ji Qin^a, Jonghyeon Ka^{a,d}, Waqas Kamal^a,
Tianxin Wang^a, Junseok Ma^{a,c,d}, Jianming Wang^a, Steve J. Elston^{a,*}, Stephen M. Morris^{a,*}

^aDepartment of Engineering Science, University of Oxford, Parks Road, Oxford OX1 3PJ, UK

^bFaculty of Mathematics and Physics, University of Ljubljana, Jadranska cesta 19, 1000 Ljubljana, Slovenia

^cNature Sciences Research Institute, KAIST, 291 Daehak-ro, Yuseong-gu, Daejeon 34141, Republic of Korea

^dDepartment of Electrical Engineering, POSTECH, Pohang 37673, Republic of Korea

*Correspondence: adithya.nair@eng.ox.ac.uk, steve.elston@eng.ox.ac.uk,
stephen.morris@eng.ox.ac.uk

March 11, 2026

Abstract

Torons are three-dimensional double-twist solitons in chiral nematic liquid crystals that form localised director configurations protected by topology and bounded by closed defect loops. They behave as particle-like entities while retaining a fully reconfigurable optical response. Here it is shown experimentally that individual torons can be created, steered and parked on demand using tailored alternating-current electric fields in planar cells, enabling deterministic control of both position and trajectory. By tuning the ratio of cell thickness to cholesteric pitch and systematically adjusting waveform parameters, including amplitude, modulation frequency, duty-cycle asymmetry and small DC offsets, robust toron nucleation is achieved and programmable translation is realised along arbitrary in-plane directions with submicrometre placement accuracy. Directional transport is controlled within a defined frequency and temperature window and can be reversed by changing modulation conditions even at zero offset. A dedicated graphical interface enables real-time switching between waveform presets so that torons follow scripted paths and draw user-defined shapes. Quantitative Landau–de Gennes Q-tensor simulations reproduce toron nucleation and the ensuing translational dynamics, supporting an interpretation in which waveform-controlled director reorientation, reorientation-driven flow and rectified polarity-sensitive coupling jointly bias the drift. Finally, three proof-of-concept functions are demonstrated: a software-defined liquid-crystal race-track memory analogue with optical readout, deterministic path writing for reconfigurable patterning, and toron-mediated pick-and-place transport of microparticles for micromanipulation.

1 Introduction

Liquid crystals (LCs) merge fluidity [1] with anisotropic molecular order [2] and thus enable a diverse range of reconfigurable soft-matter architectures [3–7]. By applying optical fields [8, 9], electric fields [10, 11] or patterned alignment [12, 13], the LC director can be programmed into distinct topological configurations that remain stable under continuous external fields [14]. These topological configurations enable a broad set of functionalities in optics, including spin-to-orbital angular momentum conversion with dynamic holography that imprints optical vortices [15], structured light emission and tunable microlasers [16], and reconfigurable photonic filters [17] and smart windows [18, 19]. Beyond optics, topological textures and defects serve as elastic templates for colloidal assembly [20] and directed particle transport [21] and as a temperature-sensitive label for transport [22].

Introducing molecular chirality into a nematic LC yields a chiral nematic (cholesteric) phase in which the helical pitch defines an intrinsic length scale and reshapes the elastic free-energy landscape [23]. Within this frustrated landscape, three-dimensional solitonic textures known as torons can form [24]: a local double-twist cylinder capped by closed disclination loops that confine the twist and suppress the associated splay and bend distortions.

A toron is a three-dimensional skyrmion-like soliton composed of a double-twist cylinder closed into a toroidal shape, with the twisted region terminated either by a pair of point defects of opposite hedgehog charge (radial $+1$ and hyperbolic -1) or by closed disclination loops, depending on boundary conditions [25]. The double-twist structure rotates the director by approximately 180° between the centre and the periphery of the toroidal cross-section, while the termination at the two point defects satisfies homeotropic surface anchoring at the confining plates [26]. Torons can be regarded as localised “atoms” of twist embedded within an otherwise nearly uniform background [27].

Traditionally, torons are generated in homeotropic cells by tightly focused, high-power laser writing of micrometre-scale structures [28]. In these geometries, the absence of a preferred in-plane axis leaves torons effectively stationary after formation, limiting applications that require controlled positioning. Here we generate torons in planar, antiparallel-rubbed cells, where the imposed director alignment introduces a well-defined in-plane directionality. Under applied alternating electric fields, this directionality enables reproducible nucleation, guided translation and precise placement of individual torons along user-programmed trajectories. Using electric fields rather than laser writing provides non-invasive and fully reversible control, allowing torons to be created, transported and erased on demand. Beyond functionality, our platform also offers a controllable route to interrogate how flexoelectric coupling [29, 30] mediates the dynamics of topological solitons in liquid crystals, using torons as a model system.

In this work, we create these torons and understand its stability in a uniform far field and elucidate electric-field-driven motion of torons and demonstrate controllable translation and placement in user-specified directions. We understand the stability of these

torons by high speed imaging. Individual torons are steered along arbitrary in-plane trajectories and positioned at chosen locations with high precision. We quantify the dependence of motion on driving frequency and temperature, measure velocities, and perform trajectory and positional-error analyses to establish accuracy and repeatability. Representative functions are shown in the figures, including racetrack-memory-style prototype and programmable microparticle transport.

2 Results

2.1 Creation of torons in liquid crystals

Torons were generated using electric fields in planar-aligned devices filled with a positive-dielectric chiral nematic mixture. The LC was confined between two antiparallel-rubbed substrates, imposing a uniform far-field director and a well-defined in-plane directionality that was later exploited for field-driven positioning. Unless stated otherwise, the chiral mixture comprised the nematic LC E7 (95.56 wt%) doped with the left-handed chiral additive S811 (5.00 wt%), with a helical pitch $p = 2.062 \mu\text{m}$ in a cell of thickness $d = 5 \mu\text{m}$ ($d/p = 2.42$). Figure 1 combines a representative voltage-driven unwinding sequence recorded for a longer-pitch sample ($p = 4 \mu\text{m}$) with pitch-dependent optical signatures and scaling trends (panels c–e).

For the sample in Fig. 1(a) ($p = 4 \mu\text{m}$, $d = 5 \mu\text{m}$ $d/p = 1.25$), the director executes approximately $d/p \approx 1.25$ full 2π rotations across the gap, producing a Grandjean texture with discrete domain walls. Under an applied AC voltage, the cholesteric initially retained a uniform helical state at 0 V (Fig. 1(a)). For a positive-dielectric-anisotropy mixture, the field favoured director alignment along the voltage axis, and the competition between dielectric torque and twist elasticity increased the effective pitch. With increasing voltage, the helix progressively unwound, and near 26 V the LC transformed into a uniform homeotropic state. In the intermediate regime, the twist walls [31] that were formed around 12 V collapsed; just below the unwinding threshold, at 4 V, this collapse created torons that emerged from this collapsing of the twist wall and persisted as localised double-twist structures. The device schematic is shown in the lower inset of Fig. 1(b), with blue arrows indicating the antiparallel rubbing directions that impose planar alignment at the substrates.

Representative visualisation of a toron under an applied electric field is shown in Fig. 1(b). The pitch window for toron formation was then established while keeping the cell gap fixed, such that the helical pitch provided the primary intrinsic length scale. To map the pitch window for toron formation, the cholesteric pitch was varied from $0.4 \mu\text{m}$ to $5.6 \mu\text{m}$ while maintaining a constant thickness of $d = 5 \mu\text{m}$. For each pitch, the applied AC voltage was swept through the same qualitative sequence of textures: a Grandjean state, a uniform linear helix appearance, and then a regime in which the twist walls shrank and collapsed as the system approached the critical unwinding into a homeotropic state. Just before this critical voltage, torons were formed as localised

double-twist objects that persisted over a finite voltage range just below the unwinding threshold. Across the dataset, toron formation was observed for pitches between $0.59\ \mu\text{m}$ and $4.71\ \mu\text{m}$, corresponding to $d/p \approx 8.4$ down to 1.06 , whereas outside this range the voltage response did not yield stable torons. Having established the formation window, the toron lateral diameter was measured as a function of pitch, revealing a clear monotonic scaling: larger pitch produced larger lateral toron size at fixed thickness, consistent with pitch setting the characteristic in-plane extent of the double-twist region. Representative polarising optical microscopy (POM) images of experimentally realised torons together with Q -tensor simulations for matched pitches are shown in Fig. 1(c), and the resulting pitch dependence of lateral diameter is summarised in Fig. 1(e).

Digital holographic microscopy (DHM) was used to quantify toron morphology. The system was configured as an off-axis Mach–Zehnder interferometer [32]: a small angular tilt between the reference and object beams at the recombination beamsplitter introduced a spatial carrier, and the resulting interference pattern was recorded as a hologram on a camera. The complex optical field was reconstructed using a single-FFT method followed by phase unwrapping [33]. Phase maps were referenced to the front-substrate plane, and amplitude maps were normalised to the background.

Figure 1(d) shows the unwrapped phase of a single toron, revealing a ring-like optical path-length modulation consistent with an effective refractive-index contrast between the toron core and the surrounding host. The colour scale encodes the optical phase, while the corresponding amplitude map delineates the lateral extent of the toron. Voltage-dependent phase and amplitude reconstructions, including three-dimensional amplitude renderings versus lateral position, capture the full evolution of the cholesteric texture under the applied field. Raw holograms acquired at successive voltages spanning the transition from the Grandjean state to toron formation further confirm the robustness of the technique.

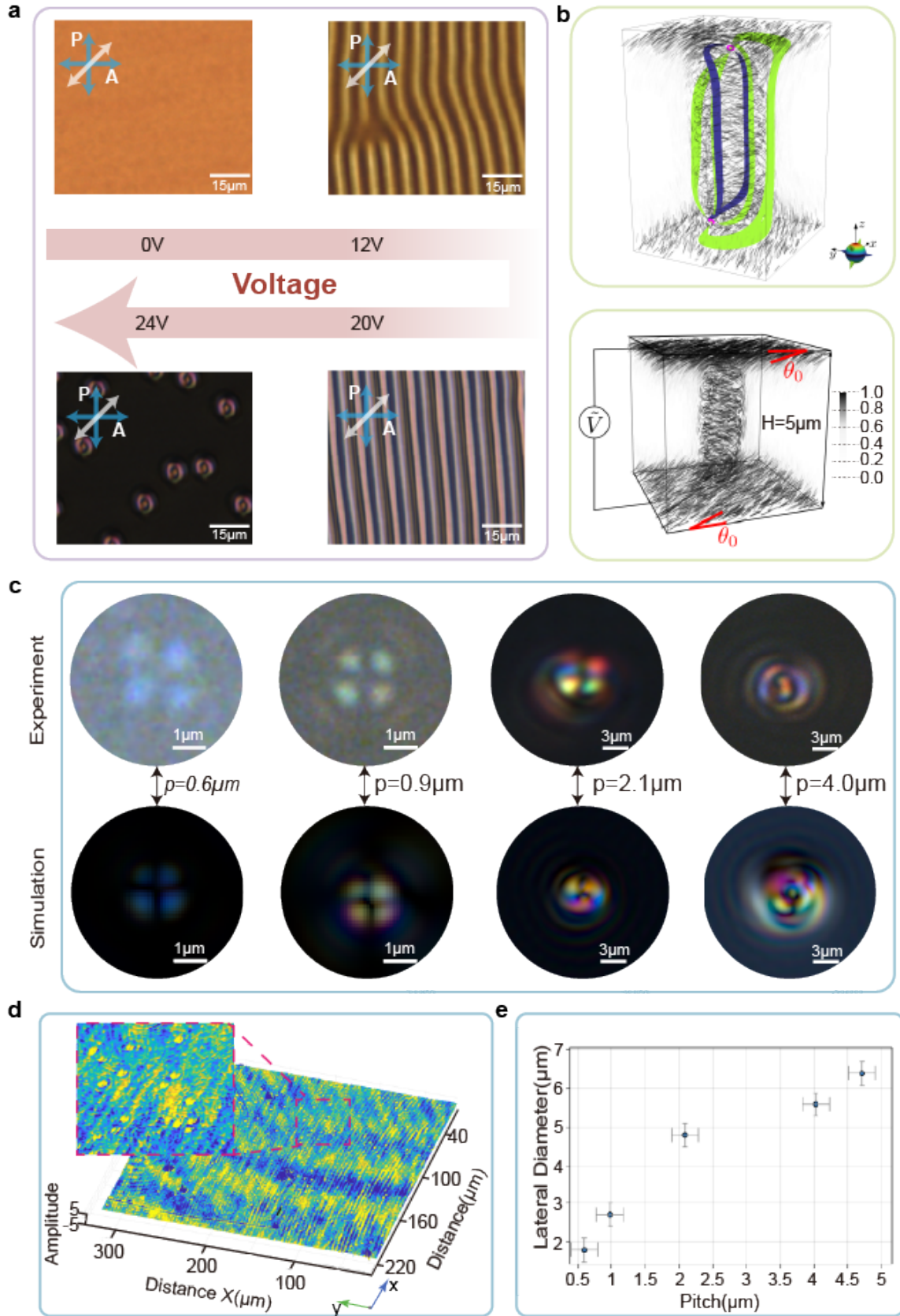


Figure 1. Voltage-induced formation and pitch-dependent scaling of torons in a confined chiral nematic cell. (a) POM micrographs at 0, 12, 20 and 24V showing the transition from a Grandjean stripe texture to isolated torons. Polariser (P) and analyser (A) directions indicated. Scale bars, $15\mu\text{m}$. (b) Numerical reconstruction of a toron: director field with coloured preimage surfaces (top) and simulation geometry, $H = 5\mu\text{m}$, under applied voltage (bottom). (c) Experimental (top) and simulated (bottom) POM textures for varying pitch p . Scale bars, $1\mu\text{m}$ (left) and $3\mu\text{m}$ (right). (d) DHM amplitude map showing the optical path-length modulation. (e) Toron lateral diameter versus pitch.

2.2 Stability

Torons remained stable under a uniform far field because stability is encoded both in their energetically favourable double-twist core and in the topological confinement provided by the accompanying defect loops. The double-twist structure locally accommodates chirality efficiently, reducing elastic penalties relative to twist distortions, while the defect loops bound the twisted region and prevent it from relaxing continuously into the surrounding background. In the present planar geometry, application of an electric field stabilises a homeotropic far field, and torons persist within this uniform background over a finite driving window. They were eliminated only when the field was driven outside this window, either restoring the uniform linear helix texture at lower drive or pushing the system towards complete unwinding at higher drive. For the mixture with pitch $p = 2.087 \mu\text{m}$, twist walls began to contract at 8 V (1 kHz) and torons formed at 12 V, before being destroyed at higher voltages as the system approached full unwinding.

The temporal robustness of these solitons under sustained driving was assessed by nucleating torons at 12 V and holding the sample at the same constant AC field for seven days. Polarising optical microscopy (POM) images recorded throughout this period showed no qualitative change in toron topology or optical signature, demonstrating long-term persistence under continuous external fields and stability within a uniform far field. Figure 2(a) summarises this stability in planar cells when the applied drive is maintained below the unwinding threshold.

To probe stability under a deliberately changing far field, high-speed microscopy was used to resolve the step-by-step response of an individual toron to an abrupt modification of the drive. Because a toron is a topological soliton, its topology, including the number of holes in the texture, is preserved under continuous deformations provided the background boundary conditions remain intact. The voltage was therefore switched off rapidly from 12 V to 0 V while recording high-speed POM images. Notably, the toron did not disappear at the instant of switch-off. Instead, it remained intact initially, while the surrounding chiral nematic background began to reorganise away from the field-stabilised homeotropic state. This far-field evolution is evident as a progressive change in POM colour and texture outside the toron, reflecting a redistribution of the director field around the soliton (Fig. 2(b)).

As this exterior director relaxation proceeds, the evolving far-field texture encroaches on the toron and progressively perturbs the boundary conditions that confine its double-twist core. Once the interference becomes sufficiently strong, topological protection can no longer be maintained within the changing background and the toron undergoes break-up. The high-speed POM sequence in Fig. 2(b) captures this pathway directly: an initially unchanged toron immediately after switch-off, followed by eventual destruction driven by reorganisation of the region beyond the soliton.

Landau-de Gennes Q -tensor simulations performed under matching conditions corroborate this interpretation. The simulated POM images in the second column of Fig. 2(b) reproduce the same sequence: following switch-off (12 V to 0 V), the toron persists while

the surrounding texture evolves, visible as a colour change outside the toron that tracks reorientation of the external director field. As relaxation continues, the simulated far field invades the soliton and triggers its eventual destruction, consistent with the experimental observations. The corresponding director-field visualisations in Fig. 2(b) further resolve the microscopic pathway, confirming that toron stability is maintained until the evolving exterior director field disrupts the confining topology and precipitates break-up.

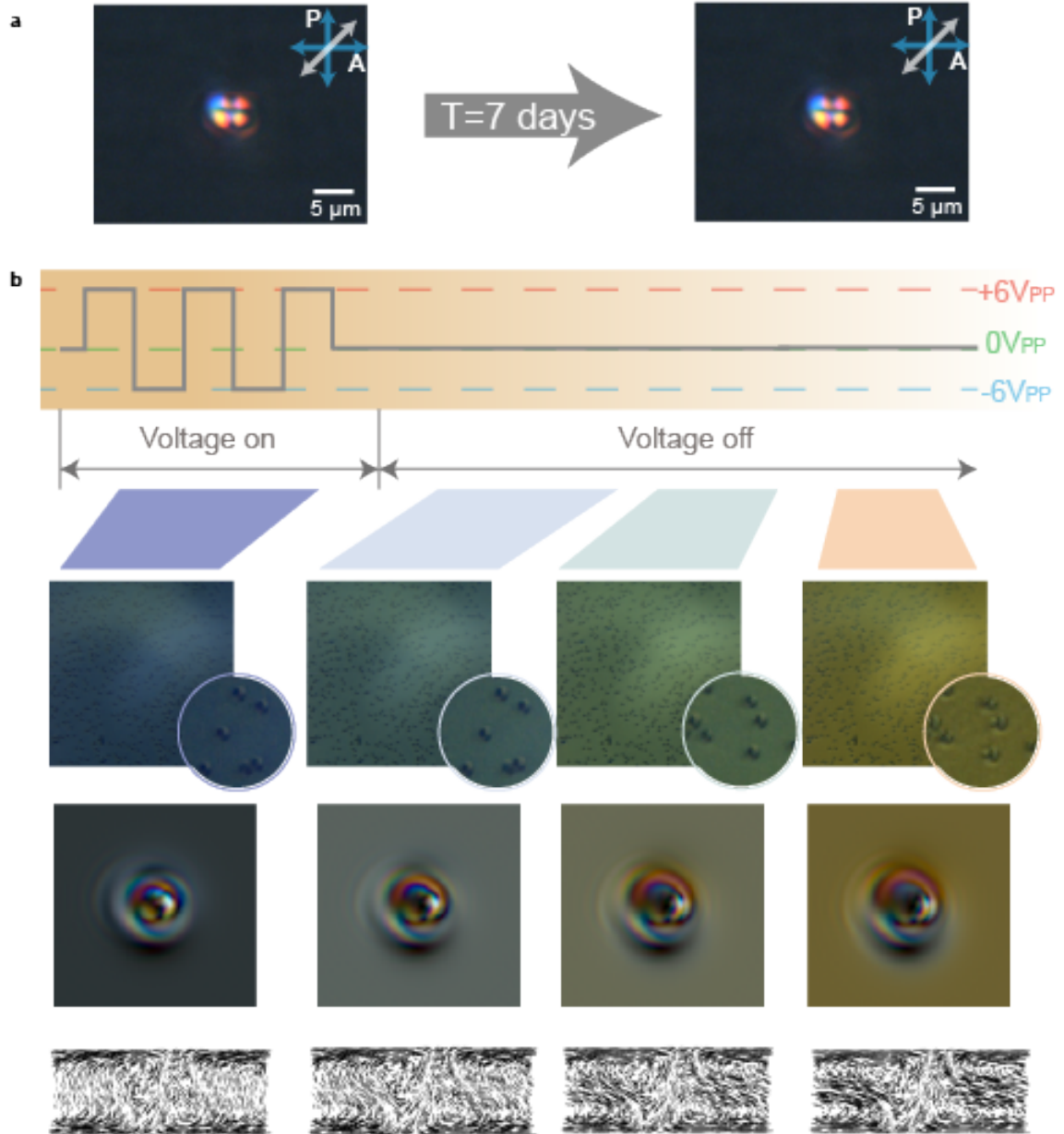


Figure 2. Field-stabilised persistence and relaxation dynamics of an isolated toron. (a) Polarising optical micrographs showing long-term stability under continuous driving, with no observable change after 7 days. (b) Relaxation following field removal. Top: applied voltage protocol ($\pm 6 V_{pp}$ square-wave drive followed by a zero-field interval). Middle: experimental POM time sequence showing the toron core persisting while the surrounding background destabilises. Bottom: corresponding Q -tensor simulations and director profiles reproducing the same relaxation pathway. Scale bars, $5 \mu\text{m}$.

2.3 Movement

Under a spatially uniform electric field, torons nucleated from twist-wall collapse remain essentially stationary. In conventional homeotropic cells this immobility is expected: the background is in-plane isotropic, with no preferred lateral axis to bias motion, so torons pin at sporadic locations set by local imperfections and nucleation history. Their positions are therefore random and irreproducible across the device, which limits applications that require deterministic placement, transport, or rewriting. By contrast, planar cells with antiparallel rubbing impose a well-defined in-plane director axis, providing the broken symmetry required for controlled, directional motion under electrical driving.

A first indication that the formation pathway itself can bias position was obtained by voltage cycling. After formation, a toron was tuned to a lower voltage at which extended twist walls reappear (10 V, 1 kHz). On reducing the drive, the localised toron elongated and relaxed back into an extended twist-wall segment; returning the voltage to 12 V then regenerated the toron, demonstrating reversibility under repeated cycling. Notably, the re-formed toron did not return to its original lateral position. Instead, each down and up voltage cycle produced a finite net in-plane displacement, revealing a lateral step associated with the formation and collapse pathway. This reproducible net shift indicates an asymmetry in the collapse and re-nucleation dynamics and provides a practical mechanism to bias toron position under otherwise spatially uniform fields.

Continuous, deterministic translation was driven by applying a temporally modulated AC waveform to the planar cell. The drive consisted of a 1 kHz sawtooth carrier whose peak amplitude was controlled by a 60 Hz sawtooth envelope that ramped from 0 V to 24 V and then reset at the start of the next cycle. This repeated sweep traversed the toron stability window and generated a net in-plane bias: individual torons translated reproducibly in a single, fixed direction across the field of view and could be repositioned along user-defined paths. Motion persisted under sustained modulation and ceased promptly when the envelope modulation was halted, even though the 1 kHz carrier remained applied. The response was repeatable across multiple runs with identical parameters, and trajectories were consistent for torons initialised at different starting locations within the same device.

A custom control interface was developed to apply prescribed voltages and waveforms during toron manipulation. The software functioned as a waveform synthesiser, enabling real-time specification of amplitude and offset, selection of waveform shape (including continuous interpolation between sawtooth and square forms), control of waveform asymmetry, and independent tuning of the carrier frequency and the low-frequency envelope modulation. Toron motion was monitored in situ by polarising optical microscopy using a CCD camera, and videos were recorded for subsequent trajectory and velocity analysis.

Under burst-modulated driving, torons exhibited a pronounced directional drift (northward in the laboratory frame for the waveform shown). As the modulation frequency was increased, the drift speed decreased and vanished at 72 Hz, where the toron became effectively stationary. Increasing the drive amplitude at fixed frequency then induced a

reversal of the drift direction, and the magnitude of the reversed velocity increased with amplitude, persisting up to 90 Hz. Beyond 90 Hz, no net translation was detected and stable torons could not be maintained under otherwise identical conditions. These trends were reproducible across repeated frequency sweeps on the same device.

Because torons emerge from the collapse of twist walls, their field response is expected to inherit key features of twist-wall electrodynamics. Twist walls exhibit a flexoelectric contribution under temporally asymmetric driving that mimics a chiral flexo-electro-optic response governed by $e_1 - e_3$ [34]. To impose an analogous bias on torons, temporal symmetry was deliberately broken in the applied waveform. Starting from a 1 kHz carrier with 60 Hz amplitude modulation and a peak of 24 V, a symmetric sawtooth (equal rise and fall, zero DC offset) produced translation perpendicular to the rubbing axis (north in the laboratory frame). The trajectory angle was then rotated by introducing waveform skew: with a rise-time fraction of 20% and a fall-time fraction of 80% (still at zero DC offset), torons translated obliquely towards the rubbing direction (north-west), demonstrating that duty-cycle asymmetry alone biases the angle of motion. Increasing the asymmetry further to a 99% rise-time fraction and adding a small DC offset of +200 mV generated translation parallel to the rubbing axis towards the west. Reversing the sawtooth skew or changing the sign of the DC offset inverted the drift towards the east. Together, rise and fall asymmetry and a small DC bias provided a compact control space for selecting the in-plane translation angle over the full 0–180° range permitted by the planar alignment, while speed and persistence remained constrained by the modulation-frequency window identified above. The response was reproducible over repeated runs, insensitive to starting position within a device, and reversible on demand by switching between waveform presets. Piecewise switching of asymmetry and offset enabled scripted trajectories including straight segments parallel or perpendicular to rubbing, oblique diagonals, and closed paths; motion ceased promptly when the envelope modulation was halted, even if the 1 kHz carrier remained applied. The dependence on waveform polarity and temporal asymmetry is consistent with a directional bias arising from the interplay between a time-asymmetric drive and the broken in-plane symmetry imposed by planar alignment, without requiring a specific microscopic mechanism.

Position control was quantified by plotting $\Delta x(t)$ and $\Delta y(t)$ for representative motion along the cardinal directions (north, south, east and west). The waveforms used were: north, a symmetric sawtooth (50% rise-time fraction) with a 60 Hz modulation frequency and a peak amplitude of 24 V; south, a symmetric sawtooth (50%) at 85 Hz with a peak amplitude of 24 V; east, a strongly asymmetric sawtooth (99% rise-time fraction) at 70 Hz with a peak amplitude of 24 V and a +200 mV DC offset; and west, an asymmetric sawtooth (1% rise-time fraction) at 70 Hz with a peak amplitude of 24 V. The resulting $\Delta x(t)$ and $\Delta y(t)$ traces were well approximated by linear trends, indicating near-constant speed over the observation window. A waveform library enabling motion in eight programmed directions is summarised in Fig. 3(b).

Trajectories were extracted from microscopy videos using a pixel-to-micrometre conversion set by a user-defined reference in the first frame, based on a single toron of known

diameter. Bright features corresponding to torons were segmented frame by frame, small spurious regions were removed, and detections near the top and bottom image margins were excluded. Centroids were linked between frames using nearest-neighbour association with a maximum permitted step to avoid identity swaps, and displacements were reported using a fixed sign convention such that motion towards image north is positive. For visual clarity, low-order polynomial guides were overlaid on $\Delta x(t)$ and $\Delta y(t)$, whereas velocities were obtained quantitatively from linear fits to the position–time segments.

Velocity analysis was used to quantify toron motility under burst-modulated driving. Instantaneous speeds were computed from successive centroid positions and converted to $\mu\text{m s}^{-1}$. Outliers were rejected if the implied single-frame jump exceeded $20 \mu\text{m}$ or if the instantaneous speed exceeded $10 \mu\text{m s}^{-1}$. Per-second mean speed was then obtained by averaging valid framewise speeds within each 1 s bin, and a trimmed mean was reported after discarding the upper 5% of per-second values. A representative mean-speed trace over a 12 s window is shown in Fig. 3(c). Figure 3(b) further demonstrates on-demand steering in all eight directions through switching between waveform presets.

To distinguish motion dominated by flow from motion dominated by flexoelectric bias, mean velocities were compared across the programmed directions. Directions chosen to emphasise flow-driven transport yielded similar speeds, for example $0.80 \mu\text{m s}^{-1}$ for northward motion at 60 Hz and $0.77 \mu\text{m s}^{-1}$ for southward motion at 85 Hz. By contrast, directions designed to accentuate flexoelectric bias exhibited a broader spread of speeds, spanning both the highest and lowest velocities observed across the set. This wider dynamic range indicates that flexoelectric contributions provide a stronger and more tunable handle on toron velocity than flow alone, although both mechanisms may act concurrently depending on the waveform and operating point.

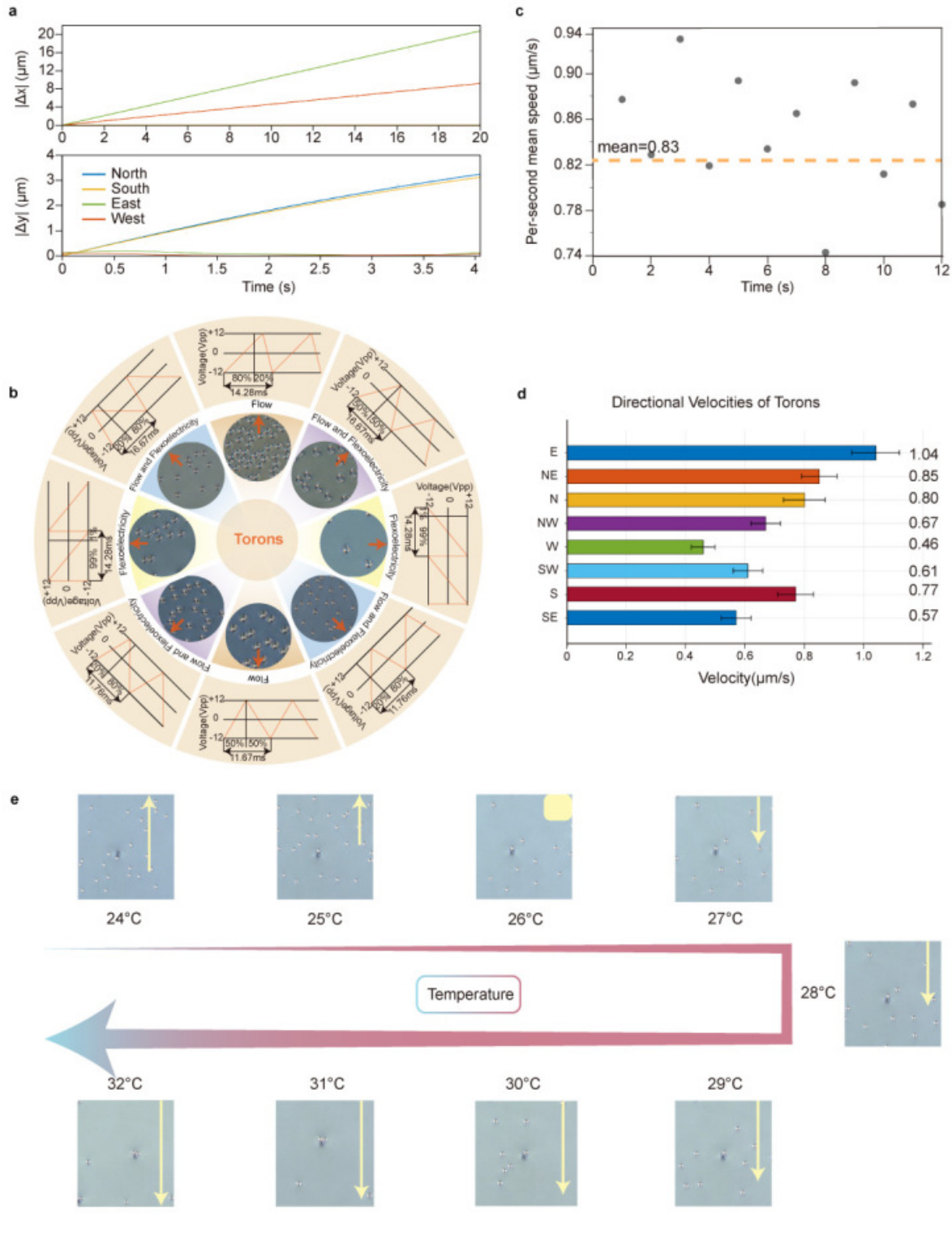


Figure 3. Programmable directional transport of torons using burst-modulated electric fields and temperature-controlled reversal. (a) Position versus time for a representative toron driven along the four cardinal directions ($\Delta x(t)$ top, $\Delta y(t)$ bottom). (b) Waveform library enabling eight-direction control. (c) Per-second mean speed over a 12s interval for the north-east trajectory; dashed line indicates the trimmed mean. (d) Mean velocities for all eight programmed directions. Error bars denote the standard error of per-second means from 12 one-second bins. (e) Temperature-controlled reversal of transport under a fixed electrical drive; images acquired in 1°C steps. All measurements used a 1 kHz carrier; “north” is defined perpendicular to the rubbing direction.

2.4 Temperature effects

All waveform-driven transport experiments described above were performed at a single room temperature, isolating how waveform parameters alone bias toron motion. Temperature dependence was then examined using the complementary protocol of holding the electrical drive fixed while varying temperature. Using a symmetric sawtooth waveform (1 kHz carrier, 60 Hz modulation, 24 V peak), torons translated north at 22 °C. The temperature was then increased from 24 °C to 34 °C in 1 °C steps with a 10 min dwell at each setpoint. Between 24 °C and 25 °C, northward motion persisted but slowed markedly. At 26 °C, net translation vanished and the toron remained effectively stationary. On further heating to 27 °C, the drift reversed and torons moved south, with speed increasing monotonically with temperature thereafter.

In parallel, the density of observable torons decreased with increasing temperature, and no torons could be sustained at or above 33 °C under these driving conditions. This temperature-driven reversal echoes the frequency-driven reversal described above, indicating that temperature shifts the same operational window that governs directional transport.

Figure 3(e) captures the same reversal when the sample is heated in 1 °C increments with a 10 min dwell at each setpoint. Varying the heating rate did not measurably alter the direction of transport: the drift direction at a given temperature and fixed waveform was the same for ramps of 1 °C per 10 min and 1 °C per 1 min. This indicates that the reversal is set primarily by the instantaneous temperature under the constant 60 Hz modulation protocol, rather than by the rate of temperature change.

2.5 Applications

This work establishes fully programmable creation, translation and erasure of individual torons in planar liquid-crystal devices, enabling deterministic positioning with sub-micrometre placement accuracy. Directional control across eight cardinal and diagonal directions, combined with GUI-scripted trajectory following, provides a general route to on-demand manipulation of stable topological solitons. In this framework, rise-fall (duty-cycle) asymmetry and small DC offsets bias the in-plane drift direction, while the modulation frequency sets the transport window and tunes the speed; notably, even with zero DC offset, changing the modulation frequency can reverse the drift direction (north to south).

These capabilities enable several practical application pathways. First, shuttling single torons between prescribed sites naturally realises racetrack-memory-style operation [35], where a soliton serves as a rewritable, mobile information carrier within a planar architecture. Second, deterministic placement of localised double-twist regions provides a reconfigurable optical building block: toron arrays could be written, translated and erased to create dynamically addressable phase and scattering landscapes for beam shaping [36], filtering or adaptive micro-optics [36, 37]. Third, toron transport offers a programmable micro-actuation mechanism for soft-matter micromanipulation, enabling controlled cap-

ture, transport and release of microparticles templated by the toron’s elastic and topological fields. Together, electrically programmable toron positioning provides a practical platform for deploying stable topological textures in liquid-crystal technologies.

For many application scenarios, sparse populations are preferred so that individual torons can be addressed and routed independently. To access this regime, a low-density distribution of torons was generated by increasing the peak amplitude above 23 V, which reduced the nucleation yield in the planar cell. A single toron was then selected and driven under GUI control. By switching between waveform presets that set the in-plane direction through duty-cycle asymmetry and a small DC offset, while maintaining a 1 kHz carrier and 60 Hz modulation, the toron was programmed to trace the letters “SMP”. The trajectory remained continuous, with accurate placement at corners and reliable turning at preset switch points, illustrating repeatable point-to-point positioning and robust path following.

Figure 4(a) shows the centroid-tracked trajectory of a single toron steered using the GUI-controlled waveform library. The reconstructed path traces the letters “SMP”, confirming on-demand control of both position and heading. Trajectories were extracted from bright-field videos by frame-by-frame centroid linking, and the overlaid track highlights faithful execution of straight segments and sharp turns, demonstrating repeatable point-to-point placement and continuous rendering of user-defined shapes.

A liquid-crystal racetrack memory analogue was realised by steering individual torons along a software-defined grid, where the occupancy of each site encodes a binary state that can be written, shifted and erased deterministically (Fig. 4(b)). In contrast to magnetic racetrack concepts [35] that rely on lithographically defined nanowires, engineered pinning sites and current-driven spin torques, the track here is virtual and reconfigurable. Torons are routed using low-voltage AC waveforms, with waveform parameters tuned to execute straight translations and 90° turns on demand through a combined contribution of director-reorientation backflow and flexoelectric bias. Bits are read optically from polarised-microscopy contrast and can be verified in real time by straightforward image segmentation.

This approach offers several practical advantages. Tracks can be reprogrammed in software without physical patterning, enabling serpentine paths, branch points and parallel lanes within the same device. The information carriers are topological solitons with long retention under constant bias, supporting low standby power. Operation is achieved at room temperature in planar ITO cells using modest amplitudes at kilohertz carrier frequencies, avoiding Joule heating and materials fatigue associated with current-driven spin devices. Together, optical readout combined with electrical write and shift, and on-the-fly reconfigurability, establishes a soft-matter racetrack platform with simple fabrication, high endurance and a natural route to dense two-dimensional arrays.

Microparticle transport was demonstrated by dispersing spacer beads in the cholesteric host and steering torons electrically as described above. The particles were nominally neutral, silica-based spacers with a diameter of $0.9\ \mu\text{m}$, which agglomerated in the LC into clusters with an apparent lateral size of approximately $4\ \mu\text{m}$. Under burst-modulated

driving, freely moving clusters were captured by nearby torons and remained bound during subsequent translation. Once loaded, a toron acted as a mobile carrier, transporting the cargo along user-selected directions set by waveform presets and releasing it at chosen locations. Figure 4(c) summarises the corresponding trajectories, highlighting pick-and-place operation and directional routing for microparticle distribution.

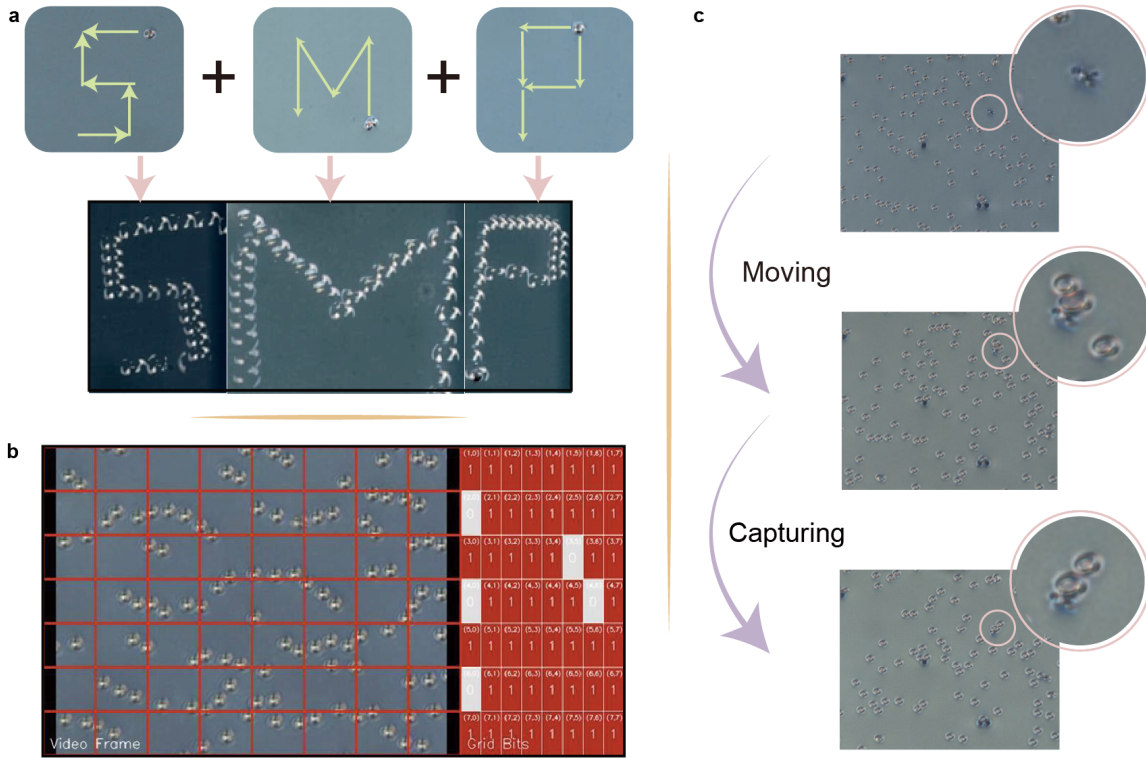


Figure 4. Proof-of-concept applications. (a) Centroid-tracked trajectory of a single toron steered to trace the letters “SMP” under GUI-controlled waveform presets. (b) Liquid-crystal racetrack memory analogue: torons written, shifted and erased along a reconfigurable virtual track with optical readout. (c) Toron-mediated microparticle pick-and-place: a silica bead cluster captured by the toron elastic field is transported and released at a target site. Scale bars, 10 μm .

3 Discussion

This work establishes an electrically driven platform for the formation, guidance and precise positioning of torons in planar liquid-crystal cells. Torons are generated without structured optical beams or high-power laser and remain stable under sustained driving within a defined operating window. Landau–de Gennes Q -tensor simulations reproduce key elements of the experimental behaviour, including toron nucleation and the observed morphologies under field, providing independent validation of the identified textures and the field–director coupling that underpins their response.

Toron creation and stability are central to the transport mechanism. In planar antiparallel rubbed cells, the applied field drives a reproducible pathway in which twist walls collapse to nucleate localised double-twist torons that persist over a finite operating win-

dow. This controlled nucleation and retention under sustained drive provide a reliable starting state for subsequent waveform-based steering.

Mean translation speeds were measured under modulated drives for motion along eight programmed directions: north (N), south (S), east (E), west (W), and the diagonals NE, NW, SE and SW. Here, “north” is defined as motion perpendicular to the rubbing axis under a symmetric sawtooth waveform at 60 Hz modulation with a 1 kHz carrier. The observed trends are consistent with two waveform-tunable contributions to the drift. First, for a sawtooth drive with zero DC offset, any polarity-sensitive cycle-averaged bias is minimised; translation is then dominated by periodic director reorientation and the associated reorientation-driven flow, yielding motion primarily along the rubbing normal (N/S). Second, introducing a strongly asymmetric duty cycle together with a small DC offset rectifies the response and produces a non-zero cycle-averaged lateral bias along the easy axis, favouring E/W motion. Diagonal trajectories arise when both components are present, with the drift direction following the vector sum of a reorientation-driven north–south component and a rectified east–west component, and the relative weights set by waveform asymmetry and offset.

Accordingly, the drive recipes were selected to weight these contributions in a controlled manner. The “Flow Up/Down” settings employ a time-balanced sawtooth (50% rise, 50% fall) with zero DC offset at 60 or 85 Hz to emphasise reorientation-driven flow, which biases motion along the rubbing normal. The “Flexo Right/Left” settings use extreme duty-cycle asymmetry (1% or 99% rise fraction) together with a small DC offset to maximise polarity-sensitive coupling and thereby bias motion along the rubbing axis. The four diagonal modes adopt intermediate duty-cycle asymmetries with zero or very small offset, producing mixed contributions that steer NE, NW, SE or SW through the vector sum of the two components.

The velocity ordering in Fig. 3(d), with E fastest and W slower than N/S, is consistent with waveform conditions that generate a larger rectified lateral component in the “Flexo Right/Left” modes than the impulse generated by the time-balanced waveform, while also highlighting that the relative weighting need not be symmetric between opposite polarities. Figure 3(b) summarises this directional control by listing the waveform parameters used to obtain each direction, including the 1 kHz carrier, modulation rate, peak voltage, duty-cycle asymmetry and any DC offset, and by indicating the dominant contribution emphasised by each recipe as defined above.

A key advance is directional programmability in a planar geometry. Using a 1 kHz carrier with low-frequency amplitude modulation, and tuning duty-cycle asymmetry together with small DC offsets, torons can be steered along any of the eight cardinal and diagonal directions with submicrometre placement accuracy. A GUI enables rapid switching between waveform presets, supporting straight translations, 90° turns, diagonals and scripted trajectories, including continuous drawing of letter shapes. These capabilities translate directly into two proof-of-concept functions. First, a liquid-crystal racetrack analogue is demonstrated in which occupancy on a software-defined grid is written, shifted and erased electrically, with optical readout and reconfigurable tracks that require no

lithographic patterning. Second, torons act as micromanipulation carriers that capture, transport and release microparticles along user-selected routes, enabling soft-matter pick-and-place at the micrometre scale. Both functions operate at room temperature using modest voltages in standard planar ITO devices.

The approach provides a practical and tunable operating envelope for electrically steerable torons. Across a wide range of frequencies and temperatures, directional transport remains robust, with the unwinding transition acting as a natural boundary that defines the accessible control space. Within this envelope, waveform parameters and material properties jointly set speed, persistence and heading, offering multiple levers including mixture composition, anchoring strength and cell geometry to boost throughput, lower drive requirements and extend scalability to large arrays. In a wider photonics context, such deterministic control over localised soft-matter states may ultimately be combined with laser-written photonic architectures, where coupling gaps and waveguide termination geometry play an important role in device performance [38, 39].

Several important questions are naturally opened by this platform. Crosstalk between neighbouring torons, many-body interactions and long-term endurance under repeated cycling remain to be quantified, and the control loop could be strengthened by closed-loop feedback using real-time imaging and automated correction of drift and placement error. Integration with patterned microelectrodes or active-matrix backplanes could enable dense two-dimensional addressability, supporting reconfigurable photonic elements, scalable memory architectures and multiplexed microrobotic transport. More broadly, the same waveform-based control framework should be transferable to other liquid-crystal topological textures, including skyrmions and hopfions, and to hybrid schemes that combine electrical steering with optical writing or readout.

In summary, electrically programmable creation, translation and erasure of individual torons in planar cells provides a general method for creation and positioning topological solitons on demand. The combination of simple fabrication, optical readout, low-voltage operation and software reconfigurability offers a practical route to liquid-crystal implementations of racetrack-style information processing, tunable photonics and micromanipulation.

4 Methods

4.1 Liquid Crystal Mixture and Cell Preparation

A left-handed cholesteric mixture was prepared by doping the nematic host E7 with the chiral additive S811 (Merck). The dopant level was selected to achieve the target helical pitch for the experiments. The mixture was introduced by capillary action into glass cells of $5\ \mu\text{m}$ gap, defined by spacer beads, at a temperature above the clearing temperature of the mixture. Both substrates carried indium tin oxide (ITO) electrodes to permit application of an electric field across the liquid crystal. Over the ITO, polyimide alignment layers were deposited and mechanically rubbed in antiparallel directions, yielding

an antiparallel-rubbed cell. Electrical leads were attached to the ITO pads and connected to a waveform generator. The completed cell was mounted on the optical platform for observation and electrical driving. No reactive mesogen or photoinitiator was used in this study, and no polymer network was formed.

4.2 Velocity Analysis

Video analysis was performed in MATLAB R2024b (MathWorks) with the Image Processing Toolbox. Movies were sampled at 60 Hz, yielding $n_F = \lfloor T \cdot 60 \rfloor$ analysed frames for a video of duration T seconds.

Spatial calibration was carried out on the first frame. A circle tightly circumscribing a single toron was drawn, and the pixel-to-length scale s was computed from the known toron diameter D as $s = D/(2R)$, where R is the drawn radius in pixels. All coordinates were scaled by s to convert to micrometres.

Each frame was converted to grayscale and binarized by adaptive thresholding with bright foreground polarity and sensitivity 0.45. Connected components smaller than 10 pixels were removed, and binary holes were filled. Object centroids were obtained from region properties. To limit edge artifacts, detections with vertical coordinate $y \leq 40$ px or $y \geq H - 40$ px, where H is the image height, were excluded.

Frame-to-frame linking used a greedy nearest-neighbour association. For each active track propagated from frame $f - 1$, the candidate centroid in frame f with the smallest Euclidean distance was accepted if the separation was less than 15 px. Unassigned detections initiated new tracks, and tracks without an assignment in the next frame were terminated.

Mean Speed Analysis Calculation

Instantaneous speed for interval $[f - 1, f]$ was computed from successive positions $\mathbf{r}_f = (x_f, y_f)$ in micrometres:

$$v_f = \frac{|\mathbf{r}_f - \mathbf{r}_{f-1}|}{\Delta t} = |\mathbf{r}_f - \mathbf{r}_{f-1}| \times 60 \mu\text{m s}^{-1} \quad (1)$$

Intervals lacking a valid association were treated as missing values.

Temporal aggregation was performed at 1 Hz by grouping consecutive sets of 60 frames into one-second bins. For bin k , the per-second mean speed \bar{v}_k was defined as the mean of all valid instantaneous speeds within that bin. Where indicated for visualization only, values smaller than $0.2 \mu\text{m s}^{-1}$ were set to NaN to suppress quiescent intervals.

Summary statistics were reported as a trimmed mean baseline \hat{v} , obtained by removing the upper 5 percent of $\{\bar{v}_k\}$ and averaging the remainder. This approach reduces sensitivity to rare mismatches during linking without relying on fixed speed thresholds.

Plots were produced in MATLAB R2024b (MathWorks) as scatter displays of \bar{v}_k versus time $t_k = k$ s with large filled markers. Axes used outward ticks, the top and right spines were hidden, and a rectangular frame was drawn. Unless stated otherwise, fixed param-

eters were: maximal link distance 15 px, excluded margins 40 px, minimum object area 10 px, trimmed-mean percentile 5 percent, and optional visualization clip at $0.2 \mu\text{m s}^{-1}$.

4.3 Single-Toron Displacement Tracking and Polynomial Fitting

Single-toron displacement analysis proceeded by selecting, after linking, the trajectory whose earliest centroid lay closest to the calibration location in the first frame. With positions recorded in micrometres as (x_i, y_i) over frames $i = 1, \dots, n$, the time axis was defined by the acquisition rate as $t_i = (i - 1)/60$ s. Displacements were referenced to the initial position and plotted with a fixed sign convention so that motion toward image north appears positive, namely

$$\Delta x_i = -(x_i - x_1), \quad \Delta y_i = -(y_i - y_1) \quad (2)$$

Intervals where the linker failed to associate a detection were left as gaps; the corresponding samples were marked missing and no interpolation across gaps was applied prior to fitting or plotting.

For presentation, each component was fitted independently with a low-order polynomial in time. Unless stated otherwise a quadratic model was used for both $\Delta x(t)$ and $\Delta y(t)$. The coefficients were obtained by least squares on the available $(t_i, \Delta x_i)$ and $(t_i, \Delta y_i)$ pairs. When the number of samples was insufficient for the requested degree, the raw displacement trace was retained without fitting. To convey the underlying measurements alongside the smooth trend, a set of evenly spaced time points was overlaid as circular markers; by default six markers were used per panel, distributed uniformly across the trace duration.

Figures displayed $\Delta x(t)$ and $\Delta y(t)$ in separate axes using box framing with outward ticks, Arial font, and grid lines disabled. Legends and titles were omitted in final layouts to preserve visual economy. Parameters held fixed across datasets, unless specified, were: frame rate 60 Hz for the time base, excluded margins 40 px and minimum object area 10 px during detection, nearest-neighbour cap 15 px for association, polynomial degree 2 for both components, and six evenly spaced sample markers.

4.4 Q -tensor simulations

We perform numerical simulations of the director field using the phenomenological Landau-de Gennes (LdG) free-energy relaxation method [40], including the liquid-crystal order parameter, elastic anisotropy, rotational viscosity, and dielectric coupling to the external electric field.

The equilibrium configuration of the director field is obtained by minimisation of the free-energy density functional, expressed in terms of the liquid-crystal order-parameter tensor

$$Q_{ij} = \frac{1}{2}S(3n_i n_j - \delta_{ij}), \quad (3)$$

where S is the scalar order parameter and \mathbf{n} is the director. The free-energy density

contains multiple contributions. The phase (Landau-expansion) part is

$$f_{\text{phase}} = \frac{1}{2}K(\partial_k Q_{ij})^2 - \frac{1}{3}\varepsilon_0\varepsilon_a^{\text{mol}} Q_{ij}E_iE_j + \frac{1}{2}A(T) \text{Tr}(Q^2) + \frac{1}{3}B \text{Tr}(Q^3) + \frac{1}{4}C[\text{Tr}(Q^2)]^2, \quad (4)$$

where the coefficient $A = a(T - T_{\text{NI}}^*)$, T is the temperature, T_{NI}^* is the supercooling temperature, and a , B , C are constant material parameters. The elastic free-energy contributions are

$$f_{\text{el}} = \frac{1}{2}L_1 \frac{\partial Q_{ij}}{\partial x_k} \frac{\partial Q_{ij}}{\partial x_k} + \frac{1}{2}L_2 \frac{\partial Q_{ij}}{\partial x_j} \frac{\partial Q_{ik}}{\partial x_k} + \frac{1}{2}L_3 \frac{\partial Q_{kl}}{\partial x_i} \frac{\partial Q_{kl}}{\partial x_j}, \quad (5)$$

$$f_{\text{chiral}} = Lq_0 \varepsilon_{ikl} Q_{ij} \frac{\partial Q_{lj}}{\partial x_k}, \quad (6)$$

$$f_{\text{diel}} = -\frac{1}{2}\varepsilon_0\bar{\varepsilon} - \frac{1}{3}\varepsilon_0\varepsilon_a^{\text{mol}} Q_{ij}E_iE_j, \quad (7)$$

where ∂_k denotes the partial derivative with respect to the k -th spatial coordinate. The first term of f_{el} represents the elastic free energy in a one-constant approximation, with K the Frank elastic constant under the isotropic elasticity assumption. The dielectric coupling constant $\varepsilon_a^{\text{mol}}$ enters both the phase and dielectric free-energy terms.

Boundary conditions were fixed to $\mathbf{n} = (\cos 85^\circ, 0, \sin 85^\circ)$ at the top and bottom surfaces, corresponding to the experimental antiparallel-rubbing geometry. The free energy was minimised using the Euler–Lagrange equation

$$\frac{\partial f}{\partial Q_{ij}} - \partial_k \frac{\partial f}{\partial (\partial_k Q_{ij})} = 0. \quad (8)$$

4.5 Polarised Optical Microscopy

Polarised microscopy imaging was carried out on an Olympus BX51 fitted with a QImaging Retiga R6 camera. Olympus objectives were used, and for each objective the cover-glass correction collar was tuned to the measured substrate thickness of the LC cell to minimise aberrations. A 550 nm long-pass filter was inserted in the illumination path to block actinic light and prevent unintended polymerisation of any residual reactive mesogen. During acquisition the polariser and analyser were kept crossed. The device was rotated until the rubbing direction lay at 45° to the polariser transmission axis, yielding a bright POM state; this orientation was kept fixed for all datasets.

Simulated POM images were generated using Nemaktis [41], an open-source Beam Propagation Method (BPM) software. Numerically computed director fields, described in the previous section, served as the input, and a broadband illumination spectrum was modelled by sampling 25 different wavelengths.

4.6 High-Speed Imaging

To characterize the temporal response and dynamic modulation behaviour of the toron when switched off, a high-time-resolution transmission microscope was constructed. A lin-

early polarized, collimated laser beam at a wavelength of 634.9 nm (THORLABS CPS635) was used as the illumination source.

The imaging system consisted of a $50\times$ objective lens with a numerical aperture of 0.50 (OLYMPUS LMPlanFI) and a tube lens with a focal length of 150 mm. In this calibration configuration, the LCCM was mounted on a precision translation stage and positioned at the sample (object) plane of the microscope, where it was directly imaged onto the camera. This arrangement allowed the spatiotemporal evolution of the speckle patterns generated by the LCCM to be measured directly. It is emphasized that this configuration was used solely for device characterization and is distinct from the illumination-modulation geometry employed in the imaging experiments described elsewhere in this work.

The modulated optical field was recorded using a high-speed camera (PHOTRON FASTCAM NOVA S6), operated at a frame rate of 20,000 frames per second with a spatial resolution of 512×512 pixels. Based on calibration with a USAF resolution target (THORLABS Negative 1951 USAF Test Target), the field of view of the imaging system was determined to be $108.1 \times 108.1 \mu\text{m}^2$. Under these conditions, the microscope provided sufficient spatial resolution to resolve speckle patterns with characteristic sizes larger than $2 \mu\text{m}$ and sufficient temporal resolution to capture speckle dynamics on timescales down to 0.05 ms.

References

- [1] E. Leslie. *Liquid Crystals: The Science and Art of a Fluid Form*. Reaktion Books, 2016.
- [2] I. C. Khoo. *Liquid Crystals*. John Wiley & Sons, 2022.
- [3] H. K. Bisoyi and Q. Li. Liquid crystals: versatile self-organized smart soft materials. *Chem. Rev.*, 122(5):4887–4926, 2021.
- [4] M. Schwartz, G. Lenzini, Y. Geng, P. B. Rønne, P. Y. Ryan, and J. P. Lagerwall. Cholesteric liquid crystal shells as enabling material for information-rich design and architecture. *Adv. Mater.*, 30(30):1707382, 2018.
- [5] R. Geryak and V. V. Tsukruk. Reconfigurable and actuating structures from soft materials. *Soft Matter*, 10(9):1246–1263, 2014.
- [6] Zhi-Chao Jiang, Yao-Yu Xiao, and Yue Zhao. Shining light on liquid crystal polymer networks: preparing, reconfiguring, and driving soft actuators. *Adv. Opt. Mater.*, 7(16):1900262, 2019.
- [7] J. Uchida, B. Soberats, M. Gupta, and T. Kato. Advanced functional liquid crystals. *Adv. Mater.*, 34(23):2109063, 2022.
- [8] M. E. McConney, A. Martinez, V. P. Tondiglia, K. M. Lee, D. Langley, I. I. Smalyukh, and T. J. White. Topography from topology: photoinduced surface features generated in liquid crystal polymer networks. *Adv. Mater.*, 25(41):5880–5885, 2013.

- [9] M. Ravnik. Topology with liquid crystals. *Physics*, 6:65, 2013.
- [10] A. Pradeep, Y. Montelongo, J. S. Ma, Z. Xu, T. Wang, J. Qin, C. Nourshargh, M. Booth, S. Elston, and S. Morris. From millimetres to microns: a hybrid strategy for reconfigurable liquid-crystal patterning. *Small Methods*, 2026.
- [11] S. Harkai, B. S. Murray, C. Rosenblatt, and S. Kralj. Electric field driven reconfigurable multistable topological defect patterns. *Phys. Rev. Res.*, 2(1):013176, 2020.
- [12] I. Nys, B. Berteloot, and G. Poy. Surface stabilized topological solitons in nematic liquid crystals. *Crystals*, 10(9):840, 2020.
- [13] B. Berteloot, I. Nys, G. Poy, J. Beeckman, and K. Neyts. Ring-shaped liquid crystal structures through patterned planar photo-alignment. *Soft Matter*, 16(21):4999–5008, 2020.
- [14] J.-S. B. Tai. Topological solitons in chiral liquid crystals. *Liq. Cryst. Today*, 32(3):45–62, 2023.
- [15] E. Brasselet and C. Loussert. Electrically controlled topological defects in liquid crystals as tunable spin-orbit encoders for photons. *Opt. Lett.*, 36(5):719–721, 2011.
- [16] M. Papič, U. Mur, K. P. Zuhail, M. Ravnik, I. Muševič, and M. Humar. Topological liquid crystal superstructures as structured light lasers. *Proc. Natl. Acad. Sci. USA*, 118(49):e2110839118, 2021.
- [17] S. Isaacs, F. Placido, and I. Abdulhalim. Investigation of liquid crystal Fabry–Perot tunable filters: design, fabrication, and polarization independence. *Appl. Opt.*, 53(29):H91–H101, 2014.
- [18] J. S. Ma, A. Pradeep, S. W. Oh, J. H. Lee, J. Y. Choi, S. O. Cha, H. W. Oh, and W. S. Kim. Operating temperature regulation in push-pull azobenzene-doped liquid crystal light-driven devices using UV absorber. *Dyes Pigm.*, page 113145, 2025.
- [19] Jun-Seok Ma, Waqas Kamal, Adithya Pradeep, Alva J Orr, Seung-Won Oh, Jin-Young Choi, Jinge Guo, Bradley Mee, Hyun-Woo Oh, Jae-Hwan Lee, et al. Advanced image-integrated smart windows using printed electrochromic polymer-dispersed liquid crystal droplets. *Advanced Optical Materials*, 13(31):e01586, 2025.
- [20] X. Wang, D. S. Miller, E. Bukusoglu, J. J. De Pablo, and N. L. Abbott. Topological defects in liquid crystals as templates for molecular self-assembly. *Nat. Mater.*, 15(1):106–112, 2016.
- [21] J. J. Sandford O’Neill, P. S. Salter, M. J. Booth, S. J. Elston, and S. M. Morris. Electrically-tunable positioning of topological defects in liquid crystals. *Nat. Commun.*, 11(1):2203, 2020.

- [22] A. Pradeep, U. Mur, J. Ma, N. Spiller, Y. Jin, W. Kamal, S. J. Elston, and S. M. Morris. Locking metastable topological domains in nematic liquid crystal Pi cells. *Adv. Funct. Mater.*, page e12550, 2025.
- [23] J.-S. Wu and I. I. Smalyukh. Hopfions, heliknotons, skyrmions, torons and both abelian and nonabelian vortices in chiral liquid crystals. *Liq. Cryst. Rev.*, 10(1-2): 34–68, 2022.
- [24] P. J. Ackerman, Z. Qi, and I. I. Smalyukh. Optical generation of crystalline, quasicrystalline, and arbitrary arrays of torons in confined cholesteric liquid crystals for patterning of optical vortices in laser beams. *Phys. Rev. E*, 86(2):021703, 2012.
- [25] I. I. Smalyukh, Y. Lansac, N. A. Clark, and R. P. Trivedi. Three-dimensional structure and multistable optical switching of triple-twisted particle-like excitations in anisotropic fluids. *Nat. Mater.*, 9(2):139–145, 2010.
- [26] J. V. Selinger. *Introduction to Topological Defects and Solitons in Liquid Crystals, Magnets, and Related Materials*. Lecture Notes in Physics. Springer, 2016.
- [27] P. J. Ackerman and I. I. Smalyukh. Reversal of helicoidal twist handedness near point defects of confined chiral liquid crystals. *Phys. Rev. E*, 93(5):052702, 2016.
- [28] C. Loussert and E. Brasselet. Multiple chiral topological states in liquid crystals from unstructured light beams. *Appl. Phys. Lett.*, 104(5), 2014.
- [29] A. Buka and N. Éber, editors. *Flexoelectricity in Liquid Crystals: Theory, Experiments and Applications*. World Scientific, 2013.
- [30] M. I. Barnik, L. M. Blinov, A. N. Trufanov, and B. A. Umanski. Flexo-electric domains in liquid crystals. *J. Phys. (Paris)*, 39(4):417–422, 1978.
- [31] R. D. Kamien and J. V. Selinger. Order and frustration in chiral liquid crystals. *J. Phys.: Condens. Matter*, 13(3):R1–R22, 2001.
- [32] Y. Liu, H. Deng, and L. Yuan. Directional torsion and strain discrimination based on Mach–Zehnder interferometer with off-axis twisted deformations. *Opt. Laser Technol.*, 120:105754, 2019.
- [33] I. Yamaguchi, T. Ida, M. Yokota, and K. Yamashita. Surface shape measurement by phase-shifting digital holography with a wavelength shift. *Appl. Opt.*, 45(29): 7610–7616, 2006.
- [34] S. J. Elston. Flexoelectricity in nematic domain walls. *Phys. Rev. E*, 78(1):011701, 2008.
- [35] R. Tomasello, E. Martinez, R. Zivieri, L. Torres, M. Carpentieri, and G. Finocchio. A strategy for the design of skyrmion racetrack memories. *Sci. Rep.*, 4(1):6784, 2014.

- [36] D. L. Shealy and J. A. Hoffnagle. Laser beam shaping profiles and propagation. *Appl. Opt.*, 45(21):5118–5131, 2006.
- [37] H. Zappe and C. Duppé, editors. *Tunable Micro-optics*. Cambridge University Press, 2015.
- [38] Ji Qin, Yunuen Montelongo, Adithya Pradeep, Zhikai Pong, Zipei Song, Tianxin Wang, Stephen M Morris, Steve J Elston, Patrick S Salter, and Martin J Booth. Termination control between collinear segments in 3d laser-written photonic circuits. In *Laser Applications Conference*, pages JW2A–5. Optica Publishing Group, 2025.
- [39] Ji Qin, Yunuen Montelongo, Adithya Pradeep, Zhikai Pong, Steve J Elston, Patrick S Salter, and Martin J Booth. Gap-controlled photonic coupling in femtosecond laser-written waveguide interconnections. *Optics Continuum*, 5(2):518–531, 2026.
- [40] M. Ravnik and S. Žumer. Landau–de gennes modelling of nematic liquid crystal colloids. *Liq. Cryst.*, 36(10–11):1201–1214, 2009.
- [41] G. Poy et al. Nemaktis: open-source beam-propagation-method software for liquid crystal optics. Accessed 2026.